Ammonia Decomposition in Electric Field over Ce-based Materials

Valeriia Maslova, Elodie Fourré, Gleb Veryasov, Nikolai Nesterenko, André Grishin, Christophe Louste, Michelle Nassar, Nadia Guignard, Sandrine Arrii, Catherine Batiot-Dupeyrat

ChemCatChem

Research Article
doi.org/10.1002/cctc.202201626

Chemistry Europe
European Chemical Societies Publishing

www.chemcatchem.org

Special Collection

Ammonia Decomposition in Electric Field over Ce-based Materials

Valeriia Maslova,[a] Elodie Fourré,[a] Gleb Veryasov,[b] Nikolai Nesterenko,[b] André Grishin,[b] Christophe Louste,[c] Michelle Nassar,[c] Nadia Guignard,[d] Sandrine Arrii,[d] and Catherine Batiot-Dupeyrat*[a]

Electric field-induced decomposition of ammonia into hydrogen and nitrogen was investigated over CeO_2, Fe-, Ru- deposited CeO_2, $CePO_4$ and Sr-doped $CePO_4$, and $CeZrO_4$ in a packed bed down-flow reactor. The effect of applied current, concentration of ammonia in a feed, and residence time was examined using CeO_2 alone. The conversion of ammonia was also studied with respect to a reduction temperature, loading and a type of the deposited metal. The activity results have been analyzed in terms of surface, morphological and electrical characterization of the catalysts. Among metal-deposited catalysts, ammonia decomposition result at 4 mA was the best for 1 wt% Fe/CeO_2 reduced at 550 °C, showing 22% of conversion with 0.18 mmol of converted ammonia per kJ of energy consumed. The activity of studied Ce-based catalysts normalized per mass of loaded catalyst showed an accordance in activity-porosity relation.

Introduction

In the past decade, ammonia, and notably green-ammonia produced from carbon-free feedstock, has gained enormous potential as it is considered as a source of zero-carbon fertilizer, fuel and energy storage. Primarily, it has the capability to impact the transition towards zero-carbon through the decarbonisation of its main use in fertiliser production. As a source to transport fuel, ammonia can be directly combusted in an engine or in a fuel cell by the reaction with air or oxygen to generate electricity. The chemical energy can be stored and transported by releasing it through direct combustion of ammonia with air or oxygen, or through decomposition to generate hydrogen.

Industrially, the conditions to crack ammonia is about 850–950 °C and nickel supported on alumina catalyst.[1] In thermal catalysis, the catalysts used in Haber-Bosh process (synthesis of ammonia) are also considered suitable in ammonia decomposition due to the micro-reversibility in heterogeneous catalysis. Thus, ruthenium and iron supported on alumina, carbon nanotubes, MgO, rare earth metals oxide, notably CeO_2 and La_2O_3, have shown the highest rates of ammonia conversion and hydrogen production.[2] However, depending on the support and promoter used, the catalytic activity can be substantially changed due to the different metal-support interaction. The catalysts with basic sites have shown the increase of ammonia decomposition. For example, it has been shown that $Cu/ZnO/Al_2O_3$ catalysts demonstrated a high activity of ammonia decomposition (10% NH_3/He) reaching total conversion at 600 °C due to the synergetic effect of small bimetallic nanoparticles and moderate acid-base properties of the support.[3] The presence of electrodonating promoters such as K, Cs, Ba have shown significant enhancement of NH_3 conversion due to the increase of support basicity.[2] Nevertheless, the effect of promoters is dictated by the type of metal and support.

Among the alternative ways of ammonia decomposition, non-thermal plasma is considered as a possible strategy. In contrast to thermal catalysis, in plasma, the process of ammonia decomposition is not at thermodynamic equilibrium, therefore being decomposed to N_2 and H_2, the ammonia synthesis rate will be reduced.[4] Plasma chemistry in Ar/NH_3 Dielectric–Barrier–Discharge (DBD) was investigated by Fateev et al. in 2005.[5] The authors showed that for low ammonia concentration from 0.1 to 3% the main processes for NH and NH_2 formation is energy exchange between Ar metastable atoms and NH_3 molecules (Penning ionization effect) while collisions of electrons with NH_3 is important for ammonia

[a] Dr. V. Maslova, Dr. E. Fourré, Prof. Dr. C. Batiot-Dupeyrat
UMR CNRS 7285 – IC2MP, Université de Poitiers
ENSIP-bat B1
1 rue Marcel Doré, TSA41105, 86073 Poitiers Cedex 9 (France)
E-mail: catherine.batiot.dupeyrat@univ-poitiers.fr
[b] G. Veryasov, N. Nesterenko, A. Grishin
TotalEnergies One Tech
(Belgium)
[c] Prof. Dr. C. Louste, Dr. M. Nassar
Institut Pprime UPR 3346
Université de Poitiers
2 Boulevard des Frères Lumière, 86360, Chasseneuil-du-Poitou (France)
[d] N. Guignard, S. Arrii
IC2MP – UMR 7285
PLATeforme INstrumentale d'Analyses
Spectroscopies Raman et UV-Visible
4 rue Michel Brunet – Bat. B27 – TSA 51106, 86073 Poitiers Cedex 9 (France)

Supporting information for this article is available on the WWW under https://doi.org/10.1002/cctc.202201626

Special Collection

This publication is part of a Special Collection on "French Conference on Catalysis 2022". Please check the ChemCatChem homepage for more articles in the collection.

concentration between 3 and 10%. Plasma-catalytic processes for NH_3 decomposition have been investigated by different groups. The main results are gathered in Table 1.

Decomposition of ammonia linearly yielded hydrogen in the study using dielectric barrier discharge (DBD) reactor with the rod or metal wool as a high voltage electrode.[6] The applied power and the residence time were significantly influencing the conversion regardless of the nature of high voltage electrode nature. Wang et al.[7] investigated the influence of reaction temperature on a FeO catalyst under plasma discharge. They achieved a complete NH_3 conversion at 410 °C while the catalyst alone gave NH_3 conversion of 7.4%.

Ruthenium nanoparticles supported on different oxides are regarded as the most performing catalysts also in plasma-induced ammonia decomposition.[8] The best results were obtained with Al_2O_3 support compared to SiO_2.

Recently, the activity of several other metals and bi-metallic nanoparticles such as Ni, Co, Fe, Mo, and Fe–Co, Mo–Co, Fe–Ni, Mo–Ni supported on fumed-silica have been tested and reported in the process with DBD reactor.[9] Among all, the catalyst Fe–Ni (Fe/Ni = 6/4 molar ratio) have shown to be the most active, leading to a complete ammonia conversion at 500 °C. The decomposition of ammonia was also studied using ferroelectric packed bed of lead zirconate titanate – $Pb[ZrxTi_{1-x}]O_3$ – in two parallel plate stainless steel electrodes.[4] One of the peculiarities of this material $Pb[ZrxTi_{1-x}]O_3$ is the capacity to incorporate hydrogen in its structure. The authors reported the dependence of ammonia decomposition on the flow rate, applied power and the feed composition. Thus, a greater conversion of pure ammonia was achieved at lower flow rate and greater applied power. While tests using the mixture of $NH_3 + N_2$ (1:2) and $NH_3 + H_2$ (2:3) showed that plasma electrons would preferentially activate ammonia over nitrogen molecules, and hydrogen interacted with plasma as efficiently as ammonia, which is in agreement with electron impact dissociation for N_2, H_2 and NH_3 (9.8 eV, 4.5 eV and 4.7 eV). El-Shafie et al.[10] showed that the smaller Al_2O_3 particle size (1 mm) yielded a higher NH_3 conversion whatever the feed flow rate (0.1–1 L/min) and voltage (from 12 to 18 kV). Recently Bogaerts et al.[11] obtained a NH_3 conversion of 15.1% with $MgAl_2O_4$ while it was only 5% for plasma alone. The authors indicate that the role of the solid with a low dielectric constant is to assist the creation of microdischarges in gas phase. The ammonia decomposition was studied over $MgTiO_3$ perovskite in DBD reactor.[12] Alike to previously mentioned works, ammonia decomposition increased with the increase of plasma power, reaching ca. 44% at 20 W power applied using a mixture of N_2:NH_3 = 40:1, total flow rate 25 sccm. The efficiency of the process resulted in 5.06 g-NH_3/kWh, which is still not attractive enough to meet industrial expectations. Ammonia decomposition was performed using a catalytic reactor filled with a 2%Ru/Al_2O_3 maintained at 450 °C coupled with a DBD membrane reactor. Pure NH_3 feed flow rate was comprised between 10 and 120 L/h with a deposited power in the range 500–700 W. However a maximum energy efficiency of 44.1% was reached.[13]

One of the ways to maximize the energy efficiency is the application of the electric field, which require less energy compared to plasma, and proceed in milder conditions, in which classical catalytic activity would be negligible.[14] This concept was used by the group of Sekine in the electric field-induced ammonia synthesis. Unlike the reaction in plasma (where nitrogen dissociation mechanism occurs with a decreased dissociation barrier through plasma-induced vibrational excitation of N_2), in the electric field so-called association mechanism takes place, meaning that nitrogen dissociation proceeds via formation of N_2H^+ intermediate promoted by proton H^+ hopping over the catalyst support under electric field. Therefore, surface H^+-coverage of support plays a key role.

Since the application of the electric field depends on the gas atmosphere, type of catalyst, temperature, etc.,[14,15] the aim of the present study was to investigate CeO_2-based materials in electric field-induced ammonia decomposition (at ambient temperature and pressure) since it was found to be active in electric field during the ammonia synthesis process. To the best of our knowledge such a study has never been reported.

Results and Discussion

Characterization of catalysts

Prior the tests, all the prepared catalysts were characterized by conventional techniques in catalysis, namely Temperature Program Reduction (TPR), X-ray Diffraction (XRD), Raman and N_2 physisorption, Scanning Electron Microscopy (SEM).

The TPR analysis has been carried out for calcined 1 wt% Fe/CeO_2 catalyst (non-reduced). Figure 1 shows a typical

Table 1. The main results obtained for NH_3 decomposition in plasma-catalytic processes from literature.

Total flow [mL min^{-1}]	Gas inlet	*P* [W]	catalyst	*T* [°C]	NH_3 conv. [%]	Ref.
100	4.87% NH_3 in N_2	50	no	room	100	[6]
40	100% NH_3	26	FeO	410	100	[7]
100	0.5% NH_3 in Ar	56	10 wt% Ru/Al_2O_3	room	60	[8]
120	100% NH_3	40	6Fe-4Ni	500	100	[9]
9	100% NH_3	23	$Pb[Zr_x\ Ti_{1-x}]O_3$	room	17	[4]
100	0.5% NH_3 in Ar	U: 12–18 kV	Al_2O_3	room	80	[10]
75	100% NH_3	21	$MgAl_2O_4$	room	15	[11]
25	2.4% NH_3 in N_2	20	$MgTiO_3$	room	44.4	[12]

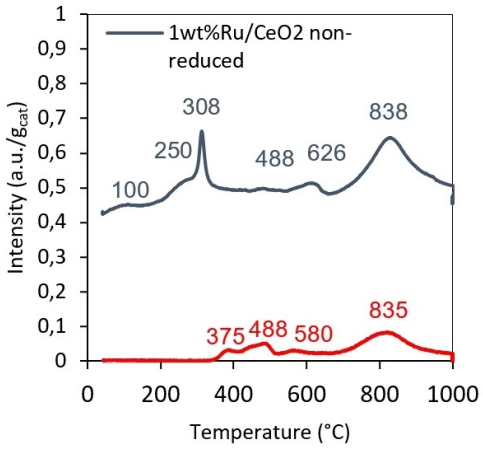

Figure 1. TPR profile as a function of temperature for non-reduced samples 1 wt% Fe/CeO_2 and 1 wt% Ru/CeO_2.

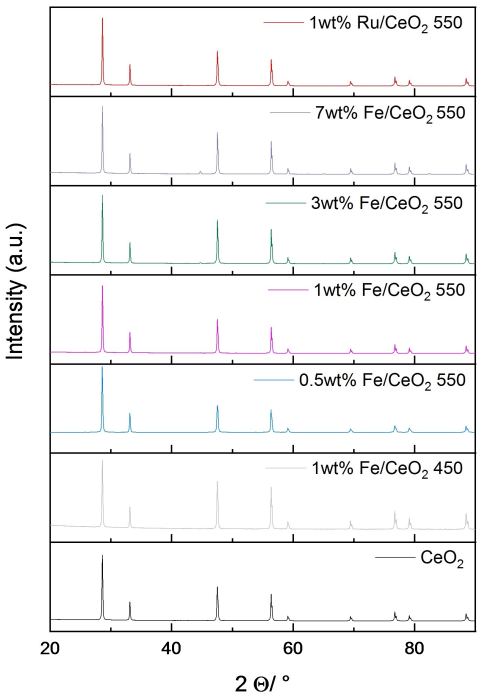

Figure 2. XRD patterns of CeO_2 and supported Fe- and Ru- catalyst reduced at 550 °C and 450 °C.

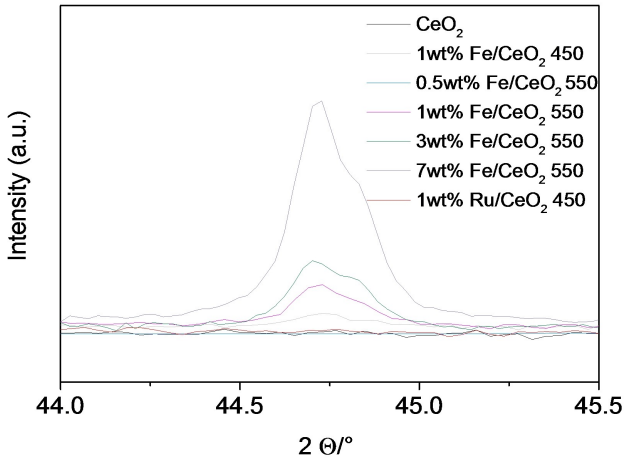

Figure 3. XRD patterns of CeO_2 and supported Fe- and Ru- catalyst reduced at 550 °C and 450 °C between 44.0 and 45.5 2Θ°.

profile for iron oxide reduction with the peaks centred at 375 °C and 488 °C attributed to $Fe_2O_3 \rightarrow Fe_3O_4$ and $Fe_3O_4 \rightarrow Fe^0$, respectively.[16] Two peaks at around 580 °C and 835 °C can be attributed to the reduction of surface lattice oxygen and bulk oxygen of CeO_2, respectively.[17] On the other hand, the peak around 488 °C is also seen in the sample of non-reduced 1wt% Ru/CeO_2, which was reported to be associated with the reduction of surface oxygen in CeO_2.[18,19] A broad peak at 100 °C could be attributed to RuO_x, which are normally reduced below 180 °C. And the peaks above 250 °C normally corresponds to the reducibility of CeO_2. Nevertheless, some other work reported that the ruthenium species were reduced in the range between 200–300 °C.[20] Therefore, 1 wt% Ru/CeO_2 sample was reduced at 450 °C and, 1 wt% Fe/CeO_2 at 450 °C and 550 °C.

Figure 2 shows the diffractograms of CeO_2 and Fe-containing CeO_2 powders. The diffractograms of all the samples corresponds to cubic fluorite structure (ICSD 98-015-5604) with the major patterns (111), (200), (220), (311), (222), (400), (331), (420), and (422) at 28.6°, 33.1°, 47.5°, 56.4°, 59.1°, 69.5°, 76.7°, 79.1° and 88.5°, respectively.

Deposition of iron over ceria in form of metal showed an appearance of diffraction at 44.7°2θ of Fe (110) starting from 1 wt% Fe gradually increasing in intensity with the loading up to 7 wt% Fe as evidenced from Figure 3. Table 2 shows that iron crystallite size (d_{Met}) of samples reduced at 550 °C is increasing with the loading of the metal from 49 for 1 wt% Fe to 85 nm for 7 wt% Fe, followed by the increase of the crystalline size of the support. This is in agreement with the decrease of surface area with the increase of iron loading. The increase of the reduction temperature did not influence significantly the crystallite size of iron, 44 nm for 450 °C and 49 nm for 550 °C.

In general, XRD demonstrate that any iron in oxide form could not be observed, and that it was deposited as large metal clusters over CeO_2. On the other hand, Ru was deposited as small lower than 3 nm particles, undetectable by XRD technique.

The XRD analysis of $CePO_4$ and Sr-doped $CePO_4$ on Figure 4 showed monoclinic $CePO_4$ (ICSD 98-007-9748). The increase of crystallite size of $CePO_4$ by Sr doping is not substantial though it is decreased as well as the surface area. The diffractogram of $CeZrO_4$ (Figure 4) prepared by auto-combustion method corresponds to cubic fluorite structure of solid solution (ICSD 98-016-5041) with the crystallite size of 6 nm. On the other hand, the separate phases were observed for $CeZrO_4$ SG, with

Table 2. The main results obtained from XRD and N_2 physisorption measurements for CeO_2 catalysts.

Catalyst	d_{CeO2} [nm]	d_{Met} [nm]*	d_{Met} [nm]**	S_{BET} [m^2/g]
CeO_2	77	–	–	2
1 wt% Fe/CeO_2 450	87	44	45	3
0.5 wt% Fe/CeO_2 550	86	–	–	1
1 wt% Fe/CeO_2 550	82	49	50	3
3 wt% Fe/CeO_2 550	87	62	61	1
7 wt% Fe/CeO_2 550	99	85	90	<1
1 wt% Ru/CeO_2 450	80	<3	<3	3

d_{Met} (nm)* iron crystallite size before reaction; d_{Met} (nm)** iron crystallite size after reaction (5% NH_3/He, 30 ml/min total flow, ambient conditions; 4 mA, 45 minutes).

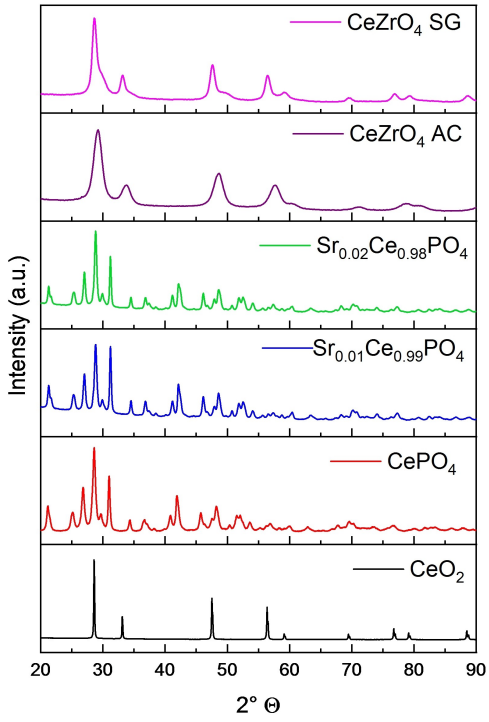

Figure 4. XRD patterns of different Ce-based catalysts.

a cubic CeO_2 (ICSD 98-015-5604) and tetragonal ZrO_2 (ICSD 98-065-5671) similar to one reported elsewhere[21] always observed for the co-precipitation synthesis at low calcination temperature. The crystallite size was found 11 nm with respect to (111) reflection of CeO_2 at 28.57°.

Scanning Electron Microscopy images showed different morphology for $CeZrO_4$ materials according to the method of synthesis used. With the auto combustion method the sample exhibited a flakes type morphology. (see Figure S1).

Samples were also characterized by the Raman spectroscopy (Figures 5). The spectrum of the fresh CeO_2 sample presented on Figure 5a demonstrates a presence of F_{2g} vibrational mode at 464 cm^{-1} corresponding to a fluorite structure of CeO_2, which is in accordance with XRD results. The magnification of the RAMAN spectrum of fresh sample also shows shifts at 260, 598 and 1174 cm^{-1}, corresponding to second order 2TA, oxygen vacancy (Frenkel defect) and second order mode 2LO, respectively.[22–24] The Raman spectra of the $Sr_{0.01}Ce_{0.99}PO_4$ and $Sr_{0.02}Ce_{0.98}PO_4$ shown on Figure 5b are identical. It presents all the vibration bands of the monoclinic $CePO_4$ structure.[25] Two bands are observed at 643 and 1016 cm^{-1} on the spectra of the Sr-$CePO_4$ samples (Figure S2), their intensities seem to increase when the Sr doping increases. These two bands are not present on the Raman spectrum of the $CePO_4$ sample. They are therefore probably due to the presence of Sr in the sample. The Raman spectrum of the $CeZrO_4$ SG sample (Figure 5c) shows a strong band at 465 cm^{-1}. This vibration corresponds to the F_{2g} mode of the fluorite structure of CeO_2. Three spectra recorded in different zones were identical. The spectrum of the $CeZrO_4$ AC sample shows three vibration bands at 310, 473 and 630 cm^{-1}, attributed to the vibrations of the $CeZrO_4$ structure.[26] The vibration at 473 cm^{-1} corresponds to the F_{2g} mode of cerium oxide, with the shift due to the contraction of the structure by incorporation of zirconium.

N_2 physisorption analysis results are collected in Table 2 and Table 3. A low surface area was found for commercial ceria with typical adsorption-desorption isotherms peculiar for non-porous solids. Other Ce-based catalysts showed a type IV isotherm inherent to mesoporous systems.

Table 3. The main results obtained from XRD and N_2 physisorption measurements for other Ce-based catalysts.

Catalyst	$d_{crys.}$* [nm]	$d_{crys.}$** [nm]	S_{BET} [m^2/g]	V_{pore} [cm^3/g]	d_{pore} [nm]
$CePO_4$	18	17	37	0.10	17
$Sr_{0.01}Ce_{0.99}PO_4$	20	18	34	0.20	28
$Sr_{0.02}Ce_{0.98}PO_4$	21	20	29	0.08	11
$CeZrO_4$ AC	6	5.5	34	0.14	26
$CeZrO_4$ SG	11	11	65	0.06	4

d_{Met} (nm)* iron crystallite size before reaction; d_{Met} (nm)** iron crystallite size after reaction (5% NH_3/He, 30 ml/min total flow, ambient conditions; 8 mA., 45 minutes).

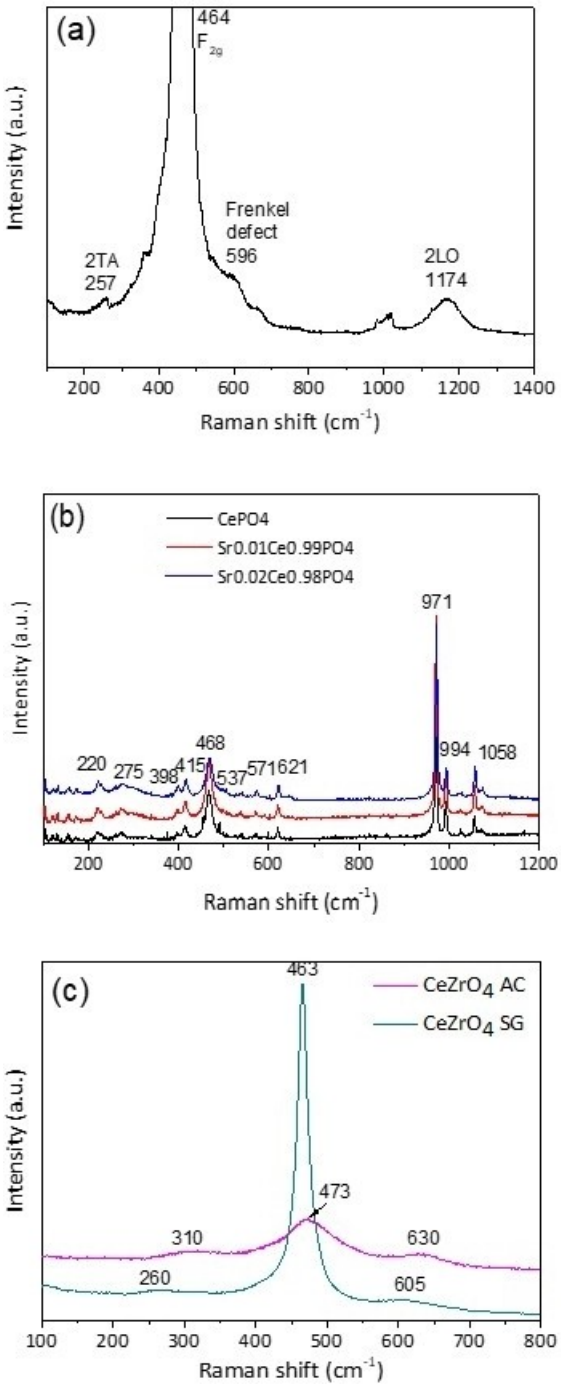

Figure 5. Raman spectra of the fresh catalysts: CeO_2 (a), $CePO_4$ and Sr-doped $CePO_4$ (b), $CeZrO_4$ mixed oxides (c).

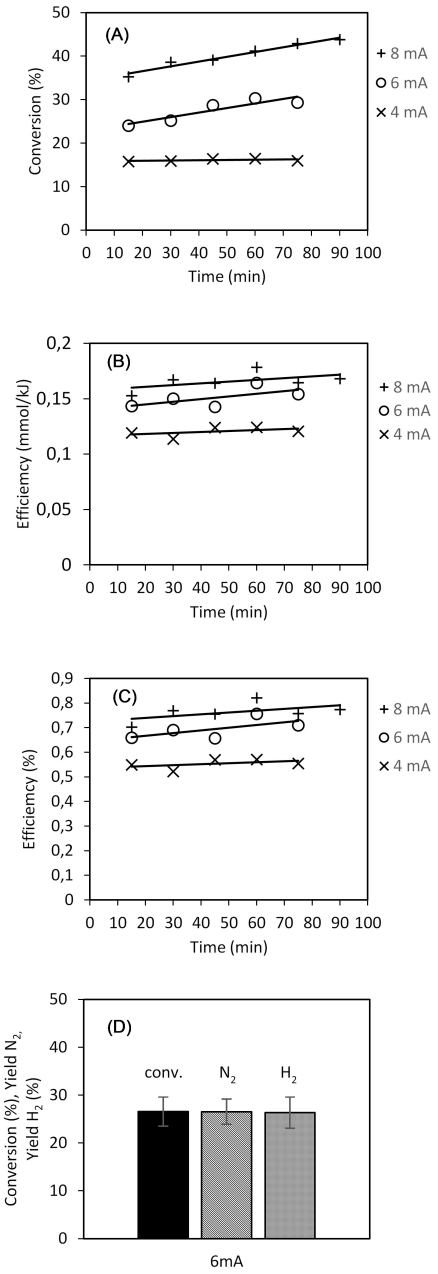

Figure 6. Ammonia decomposition over CeO_2 catalyst. Conditions: 80 mg, 5% NH_3, total flow 30 ml/min, ambient conditions; DC 4, 6 and 8 mA. (A) NH_3 conversion (%), (B) efficiency (mmol/kJ), (C) efficiency (%), (D) conversion, yield N_2 and H_2 (%).

Catalytic performance in electric field on CeO_2

Experiments were performed using CeO_2 alone in order to determine the influence of the DC applied current on ammonia decomposition (Figure 6) and to evaluate the influence of the residence time towards NH_3 conversion. The effect of ammonia concentration on decomposition was investigated for 5, 10, 20 and 30 vol%.

Decomposition of ammonia was investigated over CeO_2 at 4, 6 and 8 mA. Figure 6A–C demonstrate the evolution of conversion [Eq. (2)] and energy efficiency expressed in % and mmol/kJ [Eq. (5)] in time at different current applied. The conversion and efficiency were stable in time at 4 mA, but an increasing tendency was observed for conversion and efficiency at 6 and 8 mA.

The results shown in Figure 6D evidence that ammonia is successfully converted to nitrogen and hydrogen, and no other by-products were observed. In other published papers

the production of hydrazine under plasma was reported.[5] The blank test in the absence of the catalyst and with a quartz wool at 8 mA shown in Figure S3, demonstrate that an applied voltage of 0.49 kV and 0.51 kV instead of 0.35 kV with CeO_2 is required to obtain comparable conversion. As a result, higher efficiencies were attained when the catalyst was introduced.

To study a reason of the increase in conversion with time for tests at 6 and 8 mA, RAMAN analysis was carried out on a spent CeO_2 after test at 8 mA shown on Figure 7. Three spectra were recorded on three different areas on the surface of the sample. The spectra obtained are not identical, indicating that the sample is non-homogeneous at the microscale. The three spectra show the F_{2g} vibrational mode similar to the fresh sample (Figure 5a). The vibration bands observed at 549 and 584 cm^{-1} are associated with the presence of defects in the structure, which are more pronounced than in fresh sample. A closer look at F_{2g} bands of fresh and spent samples revealed an increase in the FWHM for used sample (13.3 cm^{-1}) compared to a fresh one (7.9 cm^{-1}). This widening could be due to an increase in crystal size and/or the formation of defects in the structure, namely oxygen vacancies[27] that could be responsible for an enhancement of the catalyst activity at higher applied currents.

The results shown in Figure 8 demonstrate that with the increase of the current, the voltage did not increase, but on the contrary decreased, suggesting the creation of a greater quantity of active species either in gas phase or on the surface of CeO_2 which could sustain the electric field. Similar observation was reported in the work of reverse water-gas shift in electric field.[15] The value of imposed voltage does not follow the Ohm's law (voltage is proportional to the resistance and current), but is dictated by the atmosphere and the electrical conductivity of the catalyst.

The effect of residence time was studied by changing the total flow rate from 15 to 40 ml/min of 5% ammonia in helium feed. Figure 9 shows the results of conversion and efficiency at a residence time of 0.10, 0.05 and 0.04 s.

The conversion of ammonia was increased with the increase of residence time. This behaviour is in accordance with the results obtained in ammonia decomposition using non-thermal plasma technology.[4,6] The efficiency of the process is decreasing with the residence time even though the input voltage for 0.10 s residence time did not result in high value as can be seen from the Figure 10. Therefore, the decrease is associated with the fact that a lower value of ammonia flow rate (corresponding to a longer residence time) is placed in numerator in the efficiency equation [Eq. (5)]. Worth noting, the voltage and conversion data shown in Figure 10 are more dispersed with a decrease of residence

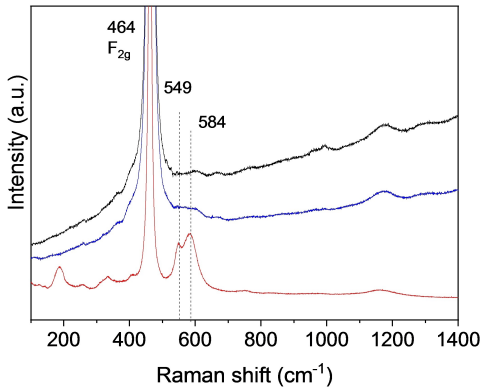

Figure 7. RAMAN spectra for used CeO_2 after test at 8 mA.

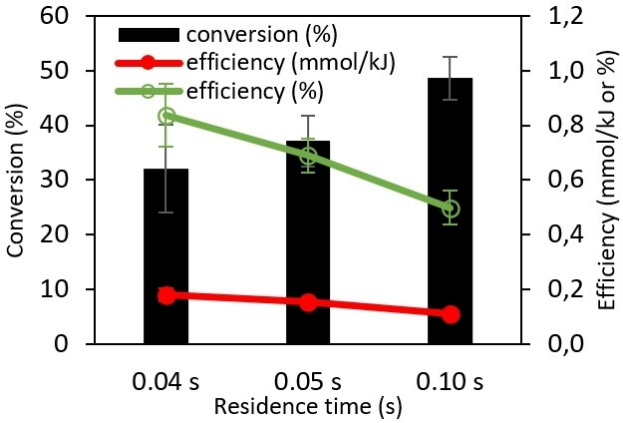

Figure 9. The effect of the residence time on ammonia decomposition over CeO_2 catalysts. Conditions: 80 mg, 5% NH_3 in Helium, ambient conditions; 8 mA, at 45 min.

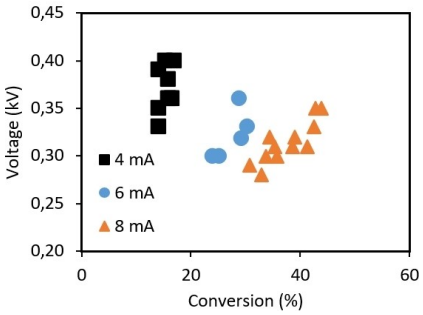

Figure 8. The dependence of conversion on voltage for different current applied. Conditions: 80 mg, 5%NH_3, total flow 30 ml/min, ambient conditions; DC 4, 6 and 8 mA, CeO_2.

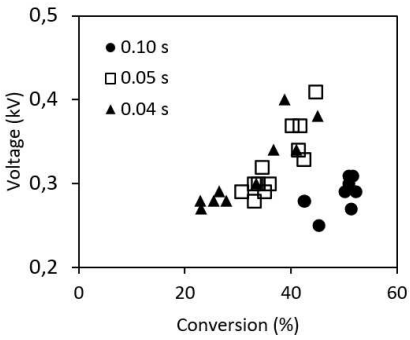

Figure 10. Dependency of voltage vs. conversion over CeO_2 catalyst. Conditions: 5% NH_3/He, ambient conditions; 8 mA.

time, indicating that higher flow in a given system may lead to perturbation and destabilization of electric field.

Comparison of different ammonia concentrations is shown in Figure 11. While the conversion does not differ substantially with the increase of concentration, the efficiency is greatly improved moving from 5 to 30% of ammonia. Further increase of ammonia concentration in feed resulted in failure to generate electric field. Similar critical purity of NH_3 on plasma generation were observed by Chang et al.[28] The work demonstrated that Penning effect between metastable argon and neutral molecules of ammonia dominates the discharge process and promotes propagation at lower ammonia flow (0.1–5.0 sccm). At a higher ammonia flow (>5 sccm) the presence of ammonia quenching effect is gradually increasing with the increase of ammonia flow rate, up to the point when plasma is no longer generated.

Catalytic activity on metal deposited CeO_2

First, the influence of reduction temperature of the deposited metal on the conversion of ammonia was studied for 1wt%Fe/CeO_2. Figure 12 demonstrate the improvement not only of the conversion and efficiency, but also on the stability of the catalyst in time (as indicated by the error bar) with the increase of temperature to 550°C. Considering that physical parameters such as crystallites size, surface area of catalysts are comparable, a better activity could result from a degree of reduction of iron and a different metal-support interaction. In addition, the test with calcined sample was performed (Figure S4) showing catalyst's deactivation with time, and suggesting that the presence of iron in reduced form on ceria is essential for ammonia decomposition in electric field. It is similar with the thermal catalytic process, many noble metals (Ru, Rh, Ir, Pt, Pd) and non-noble reduced metals (Fe, Co, Ni, Cr) deposited over various supports were successfully used for ammonia decomposition in a temperature range: 300–500°C.[2] It was proposed that the limiting step of the reaction is the N–H bond cleavage for noble metals[29] and the desorption of nitrogen for other metals.[30] The NH_3 decomposition using the combination of plasma and catalysis was studied by Yi et al.[31] The authors proposed a mechanism based on Fourier transform infrared spectroscopy and optical emission spectra characterization. It is suggested that plasma enhanced the NH_3 adsorption on Fe° and also accelerate the recombinative desorption of surface N atoms. Under electric field a similar mechanism can be suggested but further kinetic experiments are required.

The activity of ceria-supported iron was studied with respect to loading, namely, 0.5, 1, 3 and 7 wt% (Figure 13). A loading of 0.5 wt% improved the conversion and efficiency compared to ceria alone. However, 1wt%Fe was found to be an optimal loading showing a maximum for both, conversion and efficiency. A further loading decreased the conversion and efficiency drastically, in agreement with crystallites size increase and decreased of surface area. It is corroborated by the work of Gorky et al.[32] who showed a similar size effect for plasma catalytic ammonia synthesis.

In thermal catalysis as well as in plasma-catalysis ammonia decomposition, Ru-based catalysts have shown promising results.[2] With this regard, 1 wt% Ru was deposited by impregnation method and the activity was compared to 1 wt% Fe. Figure 14 shows the results of ammonia decomposition at 4 mA for CeO_2, 1 wt% Fe reduced at 550°C and 1 wt% Ru reduced at 450°C. The deposition of noble metal

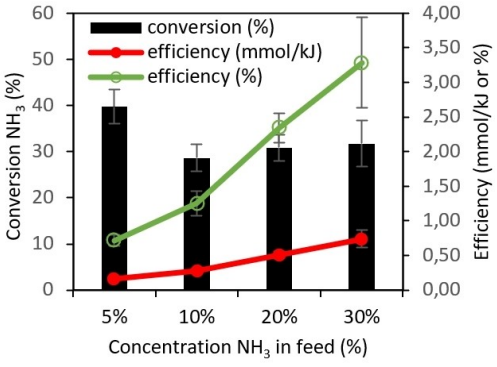

Figure 11. The effect of ammonia concentration on decomposition over CeO_2 catalysts. Conditions: 30 ml/min total flow (NH_3/He), ambient conditions; 8 mA, at 45 min.

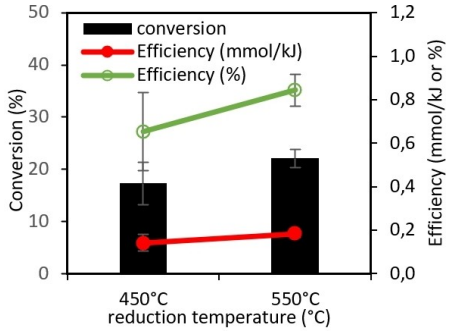

Figure 12. The effect of reduction temperature of 1 wt% Fe/CeO_2 on decomposition of ammonia. Conditions: 5% NH_3/He, 30 ml/min total flow, ambient conditions; 4 mA. Average of 60 min reactions.

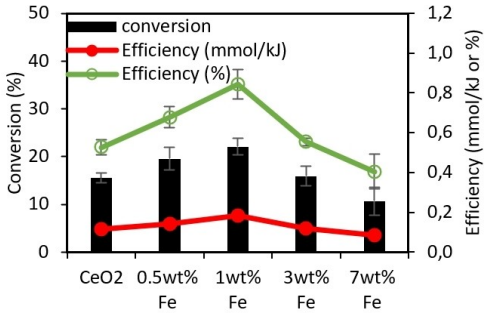

Figure 13. The effect of metal loading in the catalysts reduced at 550°C on decomposition of ammonia. Conditions: 5% NH_3/He, 30 ml/min total flow, ambient conditions; 4 mA.

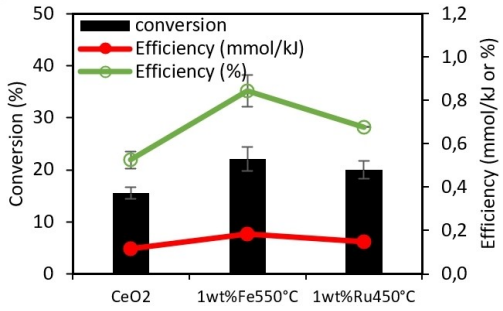

Figure 14. The effect of nature of the metal (Fe, Ru) reduced (at 550 °C and 450 °C, respectively) on decomposition of ammonia. Conditions: 5 % NH_3/He, 30 ml/min total flow, ambient conditions; 4 mA.

did not reveal an improvement of conversion, while the efficiency was decreased compared to iron catalyst.

Other cerium-containing samples

We have tested cerium in different forms, such as $CePO_4$, Sr-doped $CePO_4$ and cerium-zirconium mixed oxides prepared by two different methods: sol gel and auto combustion. Figure 15 collects the results of conversion for $CePO_4$ series of catalysts (A) and compares results of the Ce-based materials (B).

The results of conversion in time for these samples are more stable than of CeO_2 (Figure 5A). Comparing cerium phosphate series of materials, one can observe an improvement of conversion for 1 mol % Sr sample.

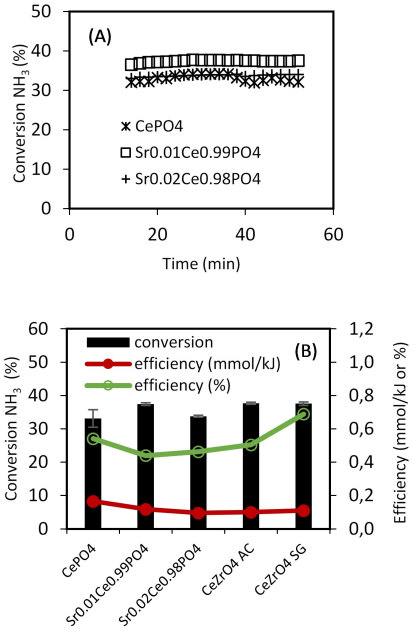

Figure 15. The effect of different Ce-based catalysts on decomposition of ammonia. Conditions: 5 % NH_3/He, 30 ml/min total flow, ambient conditions; 8 mA.

Taking into account similar surface area and crystallite size of undoped and Sr-doped $CePO_4$ (Table 3), a better conversion could result from a greater pore volume and diameter of 1 mol % Sr, whereas, it is comparable for undoped and 2 mol % Sr-doped samples. It was shown that the pore size can influence the electric field propagation inside the pores, which is more favoured for larger pores.[33] For example, in ammonia synthesis over mesoporous silica SBA-15 using non-thermal plasma in DBD reactor, the ammonia yield increased linearly with the increase of porosity.[34] The positive effect of large pores was also exhibited using BEA zeolites.[35] Indeed, $CeZrO_4$ AC with comparable surface area, volume and diameter of pores as $Sr_{0.01}Ce_{0.99}PO_4$ showed similar result of conversion. Whereas, a surface area twice as great for $CeZrO_4$ SG than $CeZrO_4$ AC could compensate its lower porosity, as these two catalytic systems showed identical performance.

The activity of catalysts normalizing per mass of catalyst [Eq. (6)] was evaluated at 8 mA since different masses were charged into the reactor to maintain 2 mm gap distance, despite all catalysts were pelletized and sieved likewise. Figure 16 demonstrate that $CeZrO_4$ AC is outperforming other catalysts once moles of ammonia converted is normalized per mass of catalyst, followed by $Sr_{0.01}Ce_{0.99}PO_4$, in accordance with activity-porosity relation. The same trend is obtained for the energy efficiency calculated per gram of catalyst. With auto combustion method, powders with flakes type morphology are produced (see Figure S1). It results in low bulk density, thus limiting the required amount of catalyst to fill up the catalytic zone between the two electrodes, with a fixed gap of 2 mm. Combustion method routes to obtain porous products with high internal pore surfaces, as shown here, were also used to produce perovskite materials.[36] The authors also indicated that combustion is a very favorable method, compared to co-precipitation or sol-gel, in terms of energy requirement for material synthesis.

The different materials used in our study differ significantly in terms of redox properties of Ce^{3+}/Ce^{4+}. The defects in CeO_2 have been mentioned as contributors to the increase in activity over time (based on Raman analysis, see above). It is known that the redox couple of Ce^{3+}/Ce^{4+} in CeO_2 improve

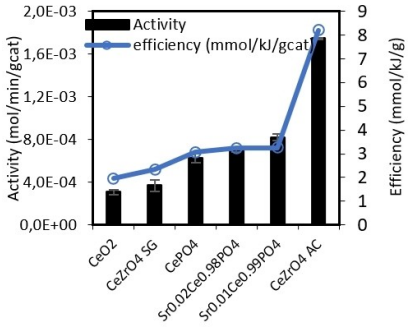

Figure 16. Comparison of different Ce-based catalysts in efficiency and activity per mass of catalyst, and corresponding permittivity values indicated by the numbers above. Conditions: 5 % NH_3/He, 30 ml/min total flow, ambient conditions; 8 mA, at 45 min.

the oxygen storage capacity and release properties due to the mobile surface and bulk oxygen.[37] The presence of oxygen vacancies in $CeZrO_4$ is also well documented into the literature.[38] On the other hand, $CePO_4$ has a stable oxidation state of Ce^{III} that cannot be oxidized to Ce (IV) thus limiting the oxygen mobility.[39]

In the present study, the catalytic activity of $CePO_4$ in terms of ammonia decomposition is relatively high compared to the other oxides possessing redox properties. So it is believed that the presence of defects in the structure does not play a key role in the decomposition of ammonia. Thus, the electrical properties of studied catalytic systems were considered.

Permittivity

To elucidate whether the dominating effect is linked to the porosity or/and to the electric properties of the catalysts, permittivity measurements were carried out and the results are presented in Table 4 and Figure S5. Permittivity shows the polarizability of the material and the interfacial space charge.

The calculations, reported elsewhere, showed that the type of plasma and its propagation inside the pores are defined by the permittivity of solids.[40,41] It has been also shown that the materials with a low permittivity value demonstrate a greater activity in plasma catalysis compared to the ones with a high value.[12,42] It is believed that with the increase of permittivity, the charge density stored in the material can be increased, however the volume of efficient discharge is reduced, and the global transformation of reactants is limited at a fixed value of deposited power. Indeed, using ferroelectric pellets ($BaTiO_3$, dielectric constant: 1 250–10 000) Gomez-Ramirez et al.[43] observed that discharges were mainly located at the contact point between pellets and electrodes, and did not extend through the whole volume. The authors also showed that plasma was ignited at lower voltages using ferroelectrics than with dielectric materials (Al_2O_3, dielectric constant: 10).

Comparing the CeO_2 and iron-deposited catalysts, at the same current of 4 mA, the conversion of ammonia is indeed improved with the decrease of permittivity. Moreover, Nyquist plot used to characterize electrical phenomena in solids,[44] depicted on Figure 17, shows a smaller semi-circle radius associated with the real part of impedance (Z′) for 1 wt% Fe/CeO_2 indicating a smaller charge-transfer resistance of the

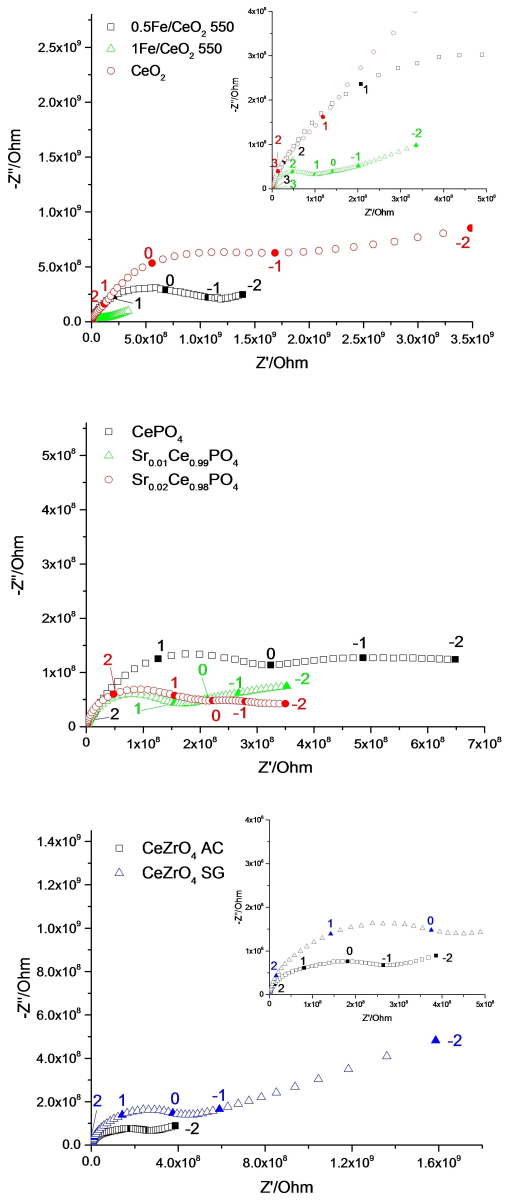

Figure 17. Nyquist EIS plots recorded in ambient air at room temperature (28 ± 2 °C) within a two-electrode electrochemical configuration. The amplitude of the applied period signal was 1 V. The logarithm of applied signal is given by numbers on diagrams.

Table 4. Permittivity results measured by electrochemical impedance spectroscopy for fresh-prepared samples. Values have been taken at 10^6 Hz with 1 V of applied signal amplitude (see Figure S4).

Catalyst	Permittivity	Conditions
CeO_2	6.5	As received
0.5 wt% Fe/CeO_2 550	5.2	Reduced at 550 °C in 10% H_2/N_2 100 ml/min
1 wt% Fe/CeO_2 550	4.3	Reduced at 550 °C in 10% H_2/N_2 100 ml/min
$CePO_4$	4.2	Calcined at 900 °C under air 100 ml/min
$Sr_{0.01}Ce_{0.99}PO_4$	2.4	Calcined at 900 °C under air 100 ml/min
$Sr_{0.02}Ce_{0.98}PO_4$	2.8	Calcined at 900 °C under air 100 ml/min
$CeZrO_4$ AC	2.9	Calcined at 600 °C under air 100 ml/min
$CeZrO_4$ SG	6.5	Calcined at 500 °C in static muffle

material.[45,46] This property could define a better conversion and energy efficiency of 1 wt% Fe/CeO_2. Giving the fact that iron-deposited commercial ceria catalysts are low surface non-porous materials, the enhanced activity is suggested to be due to the improved electrical properties.

Comparing other Ce-based materials on Figure 17, the doping of $CePO_4$ by Sr is notably reducing permittivity as well as the semi-circles showing a faster charge transfer for doped materials. Since the method of preparation is similar for $CePO_4$ and doped Sr-$CePO_4$, we do not expect a change in morphology, but the doping can improve conductivity of materials. As a matter of fact, one can notice a smaller value of permittivity and a semi-circle for 1 mol% Sr-doped $CePO_4$ which is in agreement with the results shown in Figure 15 and 16.

Similarly, comparing electrical properties of $CeZrO_4$ prepared by sol-gel and auto-combustion-prepared catalyst (Figure 17), the permittivity and the semi-circle for $CeZrO_4$ AC are smaller than for $CeZrO_4$ SG. In this case we suggest that the improved charge transfer and lower permittivity for auto-combustion method could result from the highly developed and porous morphology as shown in Figure S4, reducing a charge transfer resistance from particle-particle interactions (grain boundaries). The conversion, however, was not influenced by these properties. Therefore, one can suggest that the pore volume and surface area are a more influencing criteria than permittivity and charge transfer resistance when the porous materials are concerned. And that the ammonia decomposition in electric field is affected by the processes in gas phase (ionization, quenching, etc.) as well as on the surface and bulk of catalyst (propagation of the discharge inside the porous materials, surface catalysis, and charge transfer).

Characterization of spent catalysts

The catalysts were characterized after one hour on stream by XRD and SEM. The diffractograms did not show significant differences after reaction for the iron-based material (see Figure S6). The diffraction peak at 44.7 2Θ corresponding to Fe (110) is still clearly visible suggesting that iron remains at a metallic state after reaction. Note that in the ammonia decomposition by thermal catalysis using reduced Fe/MgO at 700 K, Lu et al.[47] showed the formation of iron mixing phase such as Fe/Fe_4N and Fe_3N which caused catalyst deactivation. The same authors proposed the use of double dielectric barrier discharge plasma to remove the surface N, which improved the catalytic performance. Under electric field the recombination of N atoms would be promoted, hindering the deposition of N atoms on Fe surface and subsequent deactivation, within one hour on stream.

The iron crystallite size was measured after reaction. The results gathered in Table 2 show that the values are not significantly modified after reaction except for 7 wt% Fe/CeO_2 whose crystallite sizes increase from 85 to 90 nm. The presence of such big crystallites being presumably responsible of the low catalytic activity.

The structural properties of the other cerium based catalyst are also not affected by the reaction. The crystallite size of $CePO_4$, $Sr_{0.01}Ce_{0.99}PO_4$, $Sr_{0.02}Ce_{0.98}PO_4$, $CeZrO_4$ SG and $CeZrO_4$ AC are not significantly modified (Table 3).

Note that the catalytic activity was very stable during one hour for those materials (Figure 15). The SEM images of $CeZrO_4$ SG and $CeZrO_4$ AC exhibit the same morphology after reaction with the presence of flake type solid for the material prepared by auto combustion (Figure S7).

Conclusion

In this work, gas phase ammonia decomposition was investigated induced by the electric field, requiring low energy inputs. The effect of applied current and residence time was more significant on the decomposition compared to the ammonia concentration in the feed. The ammonia conversion as a function of metal loading on ceria revealed an optimum value as the high metal content leads to a large metal clusters. The best result was found for 1 wt% Fe/CeO_2 reduced at 550 °C, showing 22% of conversion with 0.18 mmol of converted ammonia per kJ of energy consumed, or 0.84% energy efficiency. Following the activity-properties analysis, it seems that the electrical characteristics determine ammonia conversion in case of non-porous systems. Whereas, the porosity and surface area are more influencing criteria than permittivity and charge transfer resistance when it comes to the porous materials. Moreover we showed that cerium based oxides exhibit a high stability during one hour on stream without significant structural modification. Longer tests will have to be carried out in order to validate the interest of such materials for ammonia decomposition under electric field.

Experimental Section

This part shows the list of materials used, describes the methods of catalysis synthesis, the reactor geometry used and briefly shows the analytical conditions.

The preparation was following the procedure described by the group of Sekine.[48] In principle, the metal precursor $(Ru(C_5H_7O_2)_3$, Ruthenium (III) acetylacetonate, Sigma–Aldrich; $Fe(C_5H_7O_2)_3$, Iron (III) acetylacetonate, Sigma–Aldrich) was dissolved in acetone (100 mM). The support CeO_2 (2 g, Cerium (IV) oxide, Rectapur Prolabo) was dispersed in acetone (25 ml) and stirred for 2 h, 250 rpm, room temperature. The solution of metal precursor was added to CeO_2 suspension and stirred for another 2 h, 250 rpm, room temperature. Then, the solvent was evaporated by rotary evaporator at room temperature. The resulting solids were dried for 24 h at 120 °C. The powders were finely grinded and calcined in static muffle oven at 450 °C for 3 h, 5 °C/min. The reduction step was performed using 10% H_2/N_2 100 ml/min at 450 °C or 550 °C for 3 h, 5 °C/min. The obtained reduced catalysts were designated as 0.5 wt%, 1 wt%, 3 wt% or 7 wt% Ru/CeO_2 and Fe/CeO_2.

The preparation of $CePO_4$ was based on hydrothermal method reported elsewhere.[49] First, $Ce(NO_3)_3 \cdot 6H_2O$ (392 mg, Cerium(III)

nitrate hexahydrate, Acros Organics) and $(NH_4)_2HPO_4$ (119 mg, Diammonium phosphate, Fluka) were dissolved in water (105 mL) and stirred for 1 h at room temperature. The resulting solution was then transferred into a stainless steel autoclave with Teflon cup. After the solution was heated at 180 °C for 96 h, the precipitates were collected by filtration and washed with water (1 L). Then, the resulting precipitates were calcined at 900 °C for 3 h in 100 ml/min air flow. For the preparation of Sr-doped $CePO_4$, the certain amount of Sr precursor ($Sr(NO_3)_2$, Strontium(II) nitrate, Sigma–Aldrich) was added to the solution with Ce and P precursors in molar ratios of Sr/Ce as 1/99 and 2/98. The calcined solids were of a greenish colour, and were named as $Sr_{0.01}Ce_{0.99}PO_4$ and $Sr_{0.02}Ce_{0.98}PO_4$.

Ceria-zirconia mixed oxides were prepared by auto-combustion and sol-gel method. In auto-combustion method,[21] $Ce(NO_3)_3 \cdot 6H_2O$ (0.01 mol, Cerium(III) nitrate hexahydrate, Acros Organics) and $ZrO(NO_3)_2 \cdot xH_2O$ (0.01 mol, Zirconium(IV) oxynitrate hydrate, Sigma–Aldrich) and glycine (0.02 mol, $C_2H_5NH_2$, Merk) were dissolved in 13 ml of distilled water under stirring at room temperature. The solution was heated up to 90 °C until transparent gel is formed. The stirrer was removed, and the temperature was increased, followed by the auto-ignition, resulting in a highly spongy yellow mass. The calcination step was performed at 600 °C for 6 h 5 °C/min in air of 100 ml/min flow rate.

In sol-gel method,[50] 7.4 g of $Ce(NO_3)_3 \cdot 6H_2O$ and 3.9 g of $ZrO(NO_3)_2 \cdot xH_2O$ were dissolved in 150 ml of distilled water. An aqueous solution of NH_4OH (Ammonium hydroxide, Alfa Aesar) was slowly added dropwise under stirring (450 rpm) until pH 9.0. The resulting suspension was filtered and washed with distilled water until pH 7.0, and dried at 100 °C overnight. The calcination step was performed at 500 °C for 4 h 5 °C/min in static muffle.

XRD analyses of all the samples were carried out on diffractometer Malvern Panalytical®, Empyrean model. The source is a copper tube working with a voltage of 45 kV and a current of 40 mA. Diffractograms were recorded in the range of 10–100°2θ with a step of 0.01°2θ. Particle size determination was done by Scherrer equation over the 100% peak.

The specific surface area, pore volume and diameter of Ce-based materials was measured by N_2 physisorption technique at 77 K using TriStart 3000 Micromeritics instrument, applying single-point BET analysis (Brunauer–Emmett–Teller).

H_2-TPR of 1 wt% Fe and 1 wt% Ru on CeO_2 was carried out on Micromeritics Autochem II instrument equipped with TCD detector. The sample was first pre-treated at 200 °C for 30 min (ramp 10 °C/min) in He atmosphere. Then, the sample was cooled down to ambient temperature, and reduced in 5% H_2 /Ar (for iron) or 10% H_2/Ar (for Ru) up to 1000 °C (ramp 5 °C/min) for 60 min, 30 ml/min total flow.

RAMAN analyses were performed at room temperature with a HORIBA Jobin Yvon Labram HR 800 UV Raman confocal microscope equipped with a Peltier-cooled CCD detector. The 532 nm excitation wavelength was produced by an external laser diode (Oxxius). The laser power delivered to the sample was 0.2 mW. The spectrometer is coupled to a confocal microscope equipped with an Olympus 100x plan objective (N.A. 0.90). The size of the laser spot focused on the surface of the sample was 1 μm^2. A diffraction grating at 1800 lines/mm was used and the aperture of the confocal hole was 200 μm. The spectrometer was calibrated with a silicon standard (accuracy of 0.5 cm^{-1}). The LabSpec 5 software allowed the acquisition and processing of the results. The samples were placed directly under the microscope objective.

Electrochemical Impedance measurements of fresh samples: CeO_2, 0.5 wt% Fe/CeO_2, 1 wt% Fe/CeO_2, $CePO_4$, $Sr_{0.01}Ce_{0.99}PO_4$, $Sr_{0.02}Ce_{0.98}PO_4$, $CeZrO_4$ AC and $CeZrO_4$ SG were carried out by electrochemical impedance spectroscopy (EIS) within a two-electrode configuration at room temperature in ambient air. Two flat copper current collectors playing the role of electrodes, one of which is a guard electrode of 2 cm (3.1415 cm^2), were directly applied on both sides of the sample pellet of 3 cm of diameter and 0.558–1.335 mm of thickness, pressed by applying 5 tons of force, and dried at 40 °C in the oven during 48 hours. The thickness of each sample was measured systematically by the instrumentation installed into sample holder (Solartron) and automatically normalised so that to minimize the geometrical factor. Impedance spectroscopy measurements were performed using a Modulab Solartron Analytical potentiostat (Princeton Applied Research), in a 1–10 MHz frequency range (10 points per decade). A 1 V amplitude alternating signal was applied, with respect to the system linear behaviour.

The permittivity was found by extrapolating at 10 MHz frequency (see Figure S4) relying on a simple capacitor model [Eq. (1)]:

$$\varepsilon = \frac{C \times L}{\varepsilon_0 \times A} \quad (1)$$

where C is a capacitance automatically calculated with respect to sample thickness (L), and the surface of guard electrode (A, 3.1415 cm^2).

The morphology at a microscopic scale of $CeZrO_4$ AC and $CeZrO_4$ SG samples was examined using Scanning Electron Microscopy instrument SEM FEG JSM-7900F Jeol (5 kV, SEI detector and 6 mm working distance).

The ammonia decomposition reaction in electric field was carried out in a reactor with a point-to-plane configuration (Figure S8). A stainless steel fritted was placed over a hollow tube which is connected to the ground and previously mentioned sharp tungsten (0.5 μm) electrode as a point being a high voltage electrode. The distance between the tip of tungsten electrode and metallic fritted was fixed at 2 mm inside the Teflon connection (i.d. 4 mm). The catalyst pelletized at 5 ton and sieved in 355/630 μm grains was filled in the space of 2 mm between high voltage and ground electrodes.

The ammonia decomposition reaction was performed using NH_3 in Helium using DC high-voltage power supply (SPELMAN, SL300). The reaction was conducted at ambient temperature and pressure. The reactions for each type of catalyst were performed at least twice to confirm the reproducibility. Conversion of ammonia and Yield of products (N_2 and H_2) were calculated as follows [Eq. (2) to (4)]:

$$\text{Conversion } NH_3\ (\%) = \frac{[X(NH_3)_i - X(NH_3)_f]}{X(NH_3)_i} \times 100 \quad (2)$$

$$\text{Yield } H_2\ (\%) = \frac{\frac{2}{3} \times n(H_2,\ mol)_f}{n(NH_3,\ mol)_i} \times 100 \quad (3)$$

$$\text{Yield } N_2\ (\%) = \frac{2 \times n(N_2,\ mol)_f}{n(NH_3,\ mol)_i} \times 100 \quad (4)$$

Where $X(NH_3)_i$ and $X(NH_3)_f$ are molar fractions of ammonia in the gas mixture, initial (i) and final (f); $n(H_2,mol)_f$ and $n(N_2,mol)_f$ are moles of produced hydrogen and nitrogen, and $n(NH_3,mol)_i$ is moles of ammonia introduced.

Efficiency of the process was determined as next [Eq. (5)]:

$$\text{Efficiency } (\frac{\text{mmol}}{\text{kJ}}) = \frac{[Q_i \left(\frac{\text{mol}}{\text{min}}\right) - Q_f \left(\frac{\text{mol}}{\text{min}}\right)] \times 10^6}{60 \times \text{Power (W)}} = \frac{1}{\text{SER}} \quad (5)$$

Where Power (W or J/s) was found as a product of deposited voltage (kV) by current (mA), and Q_i and Q_f are the initial and final molar fluxes of ammonia in feed. It corresponds to the number of mole of ammonia decomposed per kJ deposited. SER: Specific Energy Required.

Another method to present the efficiency [Eq. (6)] of the process was based on the calculations suggested by Scapinello.[51] Where the enthalpy of reaction is equal to 46 kJ/mol.

$$\text{Efficiency } (\%) = 100\ \frac{\Delta H^\circ r}{\text{SER}} \quad (6)$$

Activity of the catalyst normalized by the mass of catalyst was determined as next [Eq. (7)]:

$$\text{Activity } (\frac{\text{mol}}{\text{min} \times g_{cat}}) = \frac{\text{Converted } NH_3 \left(\frac{\text{mol}}{\text{min}}\right)}{\text{mass of catalyst (g)}} \quad (7)$$

The gaseous product of reaction (essentially N_2, H_2) and unconverted ammonia was analysed online by a microGC Varian (column Volamine and helium as carrier gas).

The calibration of ammonia and nitrogen were performing by diluting the gases in helium, the two points of 10% and 5% of NH_3 were determined using the standard commercial mixture (calibration curves in Figure S9).

Acknowledgements

This work was funded by Total-Energies. We thank Celine Boissard, Julie Rousseau, and Sandrine Arii, PLATeforme INstrumentale d'Analysis of IC2MP, for assistance in SEM and XRD analyses and discussions. The authors acknowledge financial support from the European Union (ERDF) and Région Nouvelle Aquitaine. This work pertains to the French government program "Investissements d'Avenir" (EUR INTREE, reference ANR-18-EURE-0010).

Conflict of Interest

The authors declare no conflict of interest.

Data Availability Statement

The data that support the findings of this study are available from the corresponding author upon reasonable request.

Keywords: ammonia decomposition · CeO_2 · electric field

[1] A. Klerke, C. H. Christensen, J. K. Nørskov, T. Vegge, *J. Mater. Chem.* **2008**, *18*, 2304–2310.
[2] I. Lucentini, X. Garcia, X. Vendrell, J. Llorca, *Ind. Eng. Chem. Res.* **2021**, *60*, 18560–18611.
[3] V. D. B. C. Dasireddy, B. Likozar, *Fuel* **2017**, *196*, 325–335.
[4] P. Navascués, J. M. Obrero-Pérez, J. Cotrino, A. R. González-Elipe, A. Gómez-Ramírez, *ACS Sustainable Chem. Eng.* **2020**, *8*, 14855–14866.
[5] A. Fateev, F. Leipold, Y. Kusano, B. Stenum, E. Tsakadze, H. Bindslev, *Plasma Processes Polym.* **2005**, *2*, 193–200.
[6] M. Akiyama, K. Aihara, T. Sawaguchi, M. Matsukata, M. Iwamoto, *Int. J. Hydrogen Energy* **2018**, *43*, 14493–14497.
[7] L. Wang, Y. Zhao, C. Liu, W. Gong, H. Guo, *Chem. Commun.* **2013**, *49*, 3787–3789.
[8] M. El-Shafie, S. Kambara, Y. Hayakawa, *J. Energy Inst.* **2021**, *99*, 145–153.
[9] Y. Yi, L. Wang, Y. Guo, S. Sun, H. Guo, *AIChE J.* **2019**, *65*, 691–701.
[10] M. El-Shafie, S. Kambara, Y. Hayakawa, *Energy Rep.* **2020**, *6*, 25–30.
[11] J. A. Andersen, J. M. Christensen, M. Østberg, A. Bogaerts, A. D. Jensen, *Int. J. Hydrogen Energy* **2022**, *47*, 32081–32091.
[12] F. Gorky, J. M. Lucero, J. M. Crawford, B. A. Blake, S. R. Guthrie, M. A. Carreon, M. L. Carreon, *Catal. Sci. Technol.* **2021**, *11*, 5109–5118.
[13] M. El-Shafie, S. Kambara, Y. Hayakawa, *Int. J. Hydrogen Energy* **2021**, *46*, 29361–29375.
[14] Y. Hisai, Q. Ma, T. Qureishy, T. Watanabe, T. Higo, T. Norby, Y. Sekine, *Chem. Commun.* **2021**, *57*, 5737–5749.
[15] K. Oshima, T. Shinagawa, Y. Nogami, R. Manabe, S. Ogo, Y. Sekine, *Catal. Today* **2014**, *232*, 27–32.
[16] A. S. Reddy, C. Y. Chen, C. C. Chen, S. H. Chien, C. J. Lin, K. H. Lin, C. L. Chen, S. C. Chang, *J. Mol. Catal. A* **2010**, *318*, 60–67.
[17] S. Ma, S. Chen, M. Zhu, Z. Zhao, J. Hu, M. Wu, S. Toan, W. Xiang, *Int. J. Hydrogen Energy* **2019**, *44*, 6491–6504.
[18] C. Zheng, D. Mao, Z. Xu, S. Zheng, *J. Catal.* **2022**, *411*, 122–134.
[19] C. Li, Y. Shi, Z. Zhang, J. Ni, X. Wang, J. Lin, B. Lin, L. Jiang, *J. Energy Chem.* **2021**, *60*, 403–409.
[20] Y. Jin, G. Li, J. Zhang, Y. Pu, W. Li, *RSC Adv.* **2015**, *5*, 37774–37779.
[21] S. Rossignol, Y. Madier, D. Duprez, *Catal. Today* **1999**, *50*, 261–270.
[22] J. Shi, H. Li, A. Genest, W. Zhao, P. Qi, T. Wang, G. Rupprechter, *Appl. Catal. B* **2022**, *301*, 120789.
[23] S. Loridant, *Catal. Today* **2021**, *373*, 98–111.
[24] Q. Xie, H. Zhang, J. Kang, J. Cheng, Q. Zhang, Y. Wang, *ACS Catal.* **2018**, *8*, 4902–4916.
[25] A. Bouddouch, E. Amaterz, B. Bakiz, A. Taoufyq, F. Guinneton, S. Villain, J. C. Valmalette, J. R. Gavarri, A. Benlhachemi, *Optik* **2021**, *238*, 166683.
[26] K. Periyasamy, V. T. Aswathy, V. Ashok Kumar, M. Manikandan, R. Shukla, A. K. Tyagi, T. Raja, *RSC Adv.* **2015**, *5*, 3619–3626.
[27] L. Ilieva, G. Pantaleo, I. Ivanov, A. M. Venezia, D. Andreeva, *Appl. Catal. B* **2006**, *65*, 101–109.
[28] Z. S. Chang, C. W. Yao, S. Le Chen, G. J. Zhang, *Phys. Plasmas* **2016**, *23*, 093503.
[29] G. Papapolymerou, V. Bontozoglou, *J. Mol. Catal. A* **1997**, *120*, 165–171.
[30] J. C. Ganley, F. S. Thomas, E. G. Seebauer, R. I. Masel, *Catal. Lett.* **2004**, *96*, 117–122.
[31] Y. Yi, L. Wang, Y. Guo, S. Sun, H. Guo, *AIChE J.* **2019**, *65*, 691–701.
[32] F. Gorky, A. Best, J. Jasinski, B. Allen, A. Alba-Rubio, M. L. Carreon, *J. Catal.* **2021**, *393*, 369–380.
[33] S. Jo, D. H. Lee, W. S. Kang, Y. H. Song, *Phys. Plasmas* **2013**, *20*, 123507.
[34] F. Gorky, S. R. Guthrie, C. S. Smoljan, J. M. Crawford, M. A. Carreon, M. L. Carreon, *J. Phys. D* **2021**, *54*, 26.
[35] F. Gorky, M. A. Carreon, M. L. Carreon, *IOP SciNotes* **2020**, *1*, 24801.
[36] P. V. Gosavi, R. B. Biniwale, *Mater. Chem. Phys.* **2010**, *119*, 324–329.
[37] C. Larese, F. C. Galisteo, M. L. Granados, R. Mariscal, J. L. G. Fierro, P. S. Lambrou, A. M. Efstathiou, *J. Catal.* **2004**, *226*, 443–456.
[38] C. Descorme, Y. Madier, D. Duprez, *J. Catal.* **2000**, *196*, 167.
[39] S. Navarro-Jaén, L. F. Bobadilla, F. Romero-Sarria, O. H. Laguna, N. Bion, J. A. Odriozola, *J. Phys. Chem. C* **2020**, *124*, 16391–16401.
[40] Y. R. Zhang, E. C. Neyts, A. Bogaerts, *J. Phys. Chem. C* **2016**, *120*, 25923–25934.
[41] W. Wang, H. H. Kim, K. Van Laer, A. Bogaerts, *Chem. Eng. J.* **2018**, *334*, 2467–2479.
[42] N. Bouchoul, E. Fourré, A. Duarte, N. Tanchoux, C. Louste, C. Batiot-Dupeyrat, *Catal. Today* **2021**, *369*, 62–68.
[43] A. Gomez-Ramirez, R. Alvarez, P. Navascues, F. J. Garcia-Garcia, A. Palmero, J. Cotrino, A. R. Gonzalez-Elipe, *Pasma Process. Polym.* **2020**, 2000193.
[44] A. R. C. Bredar, A. L. Chown, A. R. Burton, B. H. Farnum, *ACS Appl. Energ. Mater.* **2020**, *3*, 66–98.

[45] J. Low, S. Qiu, D. Xu, C. Jiang, B. Cheng, *Appl. Surf. Sci.* **2018**, *434*, 423–432.
[46] Y. Zhang, N. Zhang, Z. R. Tang, Y. J. Xu, *ACS Sustainable Chem. Eng.* **2013**, *1*, 1258–1266.
[47] B. Lu, L. Li, M. Ren, Y. Liu, Y. Zhang, X. Tu, X. Wang, H. Qiu, *Appl. Catal. B* **2022**, *314*, 121475.
[48] K. Murakami, Y. Tanaka, S. Hayashi, R. Sakai, Y. Hisai, Y. Mizutani, A. Ishikawa, T. Higo, S. Ogo, J. G. Seo, H. Tsuneki, H. Nakai, Y. Sekine, *J. Chem. Phys.* **2019**, *151*, 064708.
[49] S. Kanai, I. Nagahara, Y. Kita, K. Kamata, M. Hara, *Chem. Sci.* **2017**, *8*, 3146–3153.
[50] C. E. Stere, J. A. Anderson, S. Chansai, J. J. Delgado, A. Goguet, W. G. Graham, C. Hardacre, S. F. R. Taylor, X. Tu, Z. Wang, H. Yang, *Angew. Chem. Int. Ed.* **2017**, *56*, 5579–5583; *Angew. Chem.* **2017**, *129*, 5671–5675.
[51] M. Scapinello, E. Delikonstantis, G. D. Stefanidis, *Chem. Eng. Process. Process Intensif.* **2017**, *117*, 120–140.

Manuscript received: December 19, 2022
Revised manuscript received: January 4, 2023
Accepted manuscript online: January 9, 2023
Version of record online: ■■, ■■■

RESEARCH ARTICLE

Electric field-induced decomposition of ammonia into hydrogen and nitrogen was performed over CeO_2, Fe-, Ru- deposited CeO_2, $CePO_4$ and Sr-doped $CePO_4$, and $CeZrO_4$; It seems that the electrical characteristics determine ammonia conversion in case of non-porous systems whereas, the porosity and surface area are more influencing criteria than permittivity when it comes to the porous materials.

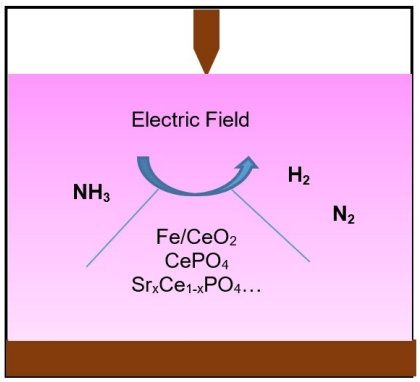

*Dr. V. Maslova, Dr. E. Fourré, G. Veryasov, N. Nesterenko, A. Grishin, Prof. Dr. C. Louste, Dr. M. Nassar, N. Guignard, S. Arrii, Prof. Dr. C. Batiot-Dupeyrat**